



AALBORG UNIVERSITY
DENMARK

Aalborg Universitet

Comparison of DC-link Voltage Control Schemes on Grid-side and Machine-side for Type-4 Wind Generation System Under Weak Grid

Huang, Liang; Wu, Chao; Zhou, Dao; Blaabjerg, Frede

Published in:

IECON 2021 – 47th Annual Conference of the IEEE Industrial Electronics Society

DOI (link to publication from Publisher):

[10.1109/IECON48115.2021.9589757](https://doi.org/10.1109/IECON48115.2021.9589757)

Publication date:

2021

Document Version

Accepted author manuscript, peer reviewed version

[Link to publication from Aalborg University](#)

Citation for published version (APA):

Huang, L., Wu, C., Zhou, D., & Blaabjerg, F. (2021). Comparison of DC-link Voltage Control Schemes on Grid-side and Machine-side for Type-4 Wind Generation System Under Weak Grid. In IECON 2021 – 47th Annual Conference of the IEEE Industrial Electronics Society (pp. 1-6)
<https://doi.org/10.1109/IECON48115.2021.9589757>

General rights

Copyright and moral rights for the publications made accessible in the public portal are retained by the authors and/or other copyright owners and it is a condition of accessing publications that users recognise and abide by the legal requirements associated with these rights.

- Users may download and print one copy of any publication from the public portal for the purpose of private study or research.
- You may not further distribute the material or use it for any profit-making activity or commercial gain
- You may freely distribute the URL identifying the publication in the public portal -

Take down policy

If you believe that this document breaches copyright please contact us at vbn@aub.aau.dk providing details, and we will remove access to the work immediately and investigate your claim.

Comparison of DC-link Voltage Control Schemes on Grid-side and Machine-side for Type-4 Wind Generation System Under Weak Grid

Liang Huang, Chao Wu, Dao Zhou, and Frede Blaabjerg

AAU Energy

Aalborg University

Aalborg East 9220, Denmark

lihu@energy.aau.dk, cwu@energy.aau.dk, zda@energy.aau.dk, fbl@energy.aau.dk

Abstract—For the type-4 wind generation system, there is a dc link in the back-to-back converter. Whether the dc-link voltage should be controlled by the grid-side converter (GSC) or machine-side converter (MSC) is still an open question, although it is usually controlled by the GSC. Considering the stability of the system mainly depends on the GSC under weak grid conditions, two typical control methods on the GSC (i.e. power control and dc voltage control) are compared in this paper. It is found that the small-signal stability of these two control schemes are basically the same when choosing the same control loop bandwidths. Even so, the power control scheme is better than the dc voltage control scheme, because a wider range is available for tuning the power loop bandwidth to improve stability. Thus, the dc voltage control carried out on the MSC should be superior to the GSC under weak grid conditions.

Keywords—small-signal stability, dc voltage control, power control, type-4 wind generation system, weak grid

I. INTRODUCTION

As the penetration rate of wind generation increases, the power grid connected to renewable energy generation is weaker than before [1], due to the larger impedance of long-distance transmission lines. This weak grid condition will cause severe voltage deviation at the point of common coupling (PCC) and some instability issues. For type-4 wind generation systems, the generator is connected to the grid via a back-to-back converter. Under weak grid conditions, the stability of this kind of wind generation system mainly depends on the grid-side converter (GSC), so the stability of GSC has attracted a lot of research attentions [2]-[5].

For the type-4 wind generation system, there is not a dc voltage source on the dc-link to provide a constant voltage, so the dc-link voltage needs to be controlled by either the MSC or the GSC [6]. Two typical dc-link voltage control schemes are introduced in [7]. One is that the dc voltage is always controlled by the GSC, while the maximum power point tracking (MPPT) is realized on the machine-side converter (MSC). The other is that the dc voltage is controlled by the GSC initially when the wind speed is very slow, but in the case that the wind speed is higher than a certain value, the dc voltage is controlled by the MSC. Thus, the MPPT is realized on the GSC by controlling the output power. Because the stability of the system mainly depends on the GSC under weak grid conditions, the MSC can be considered as an ideal source. Thus, the comparison of these two control schemes on the GSC is an interesting research topic.

At present, the small-signal stability of the power control scheme on the GSC has been studied a lot [3]-[5], so the

impact of the active power control loop, the AC voltage magnitude control loop, and the phase-locked loop (PLL) on stability is basically clear. Relatively, the studies about the small-signal stability of the dc voltage control scheme are not sufficient yet. Only a few papers [8]-[10] analyzed the small-signal stability of the dc voltage control scheme, but the difference between the dc voltage control and the power control schemes has not been investigated.

Overall, most existing papers only analyze the stability of either the power control scheme [3]-[5] or the dc voltage control scheme [8]-[10], while the difference between these two control schemes has not been investigated sufficiently. Recently, it is reported in [11] and [12] that the small-signal stability of the dc voltage control scheme is not as good as that of the power control scheme, but the precondition for the comparison is not very clear. It should be notable that if the control parameters (e.g. the power control loop and dc voltage control loop bandwidths) are not the same, the comparison would be unfair. In this paper, it is revealed that the difference between the small-signal models of these two control schemes is very tiny. Moreover, the small-signal stability of these two control schemes is almost the same when choosing the same control loop bandwidths.

Furthermore, this paper reveals that the main difference between the two control schemes is the available range for designing the bandwidths of power control loop and dc voltage control loop. For the dc voltage control scheme, the dc voltage loop bandwidth cannot be designed too low when considering the overvoltage problem on the dc-link capacitor. Namely, a higher dc voltage loop bandwidth is beneficial to avoid the overvoltage problem, but it might jeopardize the stability. Therefore, the design of the dc voltage control loop bandwidth needs a trade-off between the stability and the overvoltage problem. However, for the power control scheme, there is no such an overvoltage problem to limit the power loop bandwidth. Thus, a lower power loop bandwidth can be designed for improving stability under weak grid conditions. Hence, based on the above analyses, the power control scheme should be better than the dc voltage control scheme on the GSC under weak grid conditions.

The rest of this paper is organized as follows. Section II introduces the configurations of two typical control schemes for type-4 wind generation systems. Then, the small-signal impedance models of two control schemes are established respectively. Section III compares the stability of these two control schemes. In Section IV, the performance of these two control schemes is compared further by simulation. Finally, this paper is concluded in Section V.

$$\begin{bmatrix} \Delta v_{cd} \\ \Delta v_{cq} \end{bmatrix} - \begin{bmatrix} \Delta v_{od} \\ \Delta v_{oq} \end{bmatrix} = \begin{bmatrix} sL_f + R_f & -\omega L_f \\ \omega L_f & sL_f + R_f \end{bmatrix} \cdot \begin{bmatrix} \Delta i_{cd} \\ \Delta i_{cq} \end{bmatrix} \quad (3)$$

where “ s ” represents the Laplace differential operator in the frequency domain.

The small-signal linearized expressions of the coordinate transformation between the grid d - q frame and the control d - q frame are given by (4)-(6).

$$\begin{bmatrix} \Delta v_{od}^{ctrl} \\ \Delta v_{oq}^{ctrl} \end{bmatrix} = \begin{bmatrix} \Delta v_{od} \\ \Delta v_{oq} \end{bmatrix} + \begin{bmatrix} v_{oq0} \\ -v_{od0} \end{bmatrix} \cdot \Delta \theta_{pll} \quad (4)$$

$$\begin{bmatrix} \Delta i_{cd}^{ctrl} \\ \Delta i_{cq}^{ctrl} \end{bmatrix} = \begin{bmatrix} \Delta i_{cd} \\ \Delta i_{cq} \end{bmatrix} + \begin{bmatrix} i_{cq0} \\ -i_{cd0} \end{bmatrix} \cdot \Delta \theta_{pll} \quad (5)$$

$$\begin{bmatrix} \Delta v_{cd} \\ \Delta v_{cq} \end{bmatrix} = \begin{bmatrix} \Delta v_{cd}^{ctrl} \\ \Delta v_{cq}^{ctrl} \end{bmatrix} + \begin{bmatrix} -v_{cq0} \\ v_{cd0} \end{bmatrix} \cdot \Delta \theta_{pll} \quad (6)$$

Besides, the small-signal expression of the PLL in the control d - q frame is given by (7).

$$\Delta \theta_{pll} = (K_{p_pll} + \frac{1}{s} \cdot K_{i_pll}) \cdot \frac{1}{sV_o} \cdot \Delta v_{oq}^{ctrl} \quad (7)$$

According to (4) and (7), the expression of $\Delta \theta_{pll}$ can be derived as:

$$\Delta \theta_{pll} = \frac{K_{p_pll}s + K_{i_pll}}{s^2 + K_{p_pll}s + K_{i_pll}} \cdot \frac{1}{V_o} \cdot \Delta v_{oq} = \frac{G_{pll}}{V_o} \cdot \Delta v_{oq} \quad (8)$$

where $K_{p_pll} = 2 \cdot \zeta \cdot \omega_n$, $K_{i_pll} = \omega_n^2$. Notably, ζ is the damping ratio of the second-order system, and ω_n is the natural angular frequency of the second-order system, which is proportional to the bandwidth of the PLL if the damping ratio ζ is given.

In the steady-state, v_{od0} is equal to V_o , and v_{oq0} is equal to 0. Thus, according to (4) and (8), the expression of Δv_{odq}^{ctrl} can be deduced as:

$$\begin{bmatrix} \Delta v_{od}^{ctrl} \\ \Delta v_{oq}^{ctrl} \end{bmatrix} = \begin{bmatrix} \Delta v_{od} \\ \Delta v_{oq} \end{bmatrix} - \begin{bmatrix} 0 & 0 \\ 0 & G_{pll} \end{bmatrix} \cdot \begin{bmatrix} \Delta v_{od} \\ \Delta v_{oq} \end{bmatrix} \quad (9)$$

According to (5) and (8), the expression of Δi_{cdq}^{ctrl} can be obtained as:

$$\begin{bmatrix} \Delta i_{cd}^{ctrl} \\ \Delta i_{cq}^{ctrl} \end{bmatrix} = \begin{bmatrix} \Delta i_{cd} \\ \Delta i_{cq} \end{bmatrix} - \begin{bmatrix} 0 & \frac{-i_{cq0}}{V_o} \cdot G_{pll} \\ 0 & \frac{i_{cd0}}{V_o} \cdot G_{pll} \end{bmatrix} \cdot \begin{bmatrix} \Delta v_{od} \\ \Delta v_{oq} \end{bmatrix} \quad (10)$$

Similarly, according to (6) and (8), the expression of Δv_{cdq} can be obtained as:

$$\begin{bmatrix} \Delta v_{cd} \\ \Delta v_{cq} \end{bmatrix} = \begin{bmatrix} \Delta v_{cd}^{ctrl} \\ \Delta v_{cq}^{ctrl} \end{bmatrix} + \begin{bmatrix} 0 & \frac{-v_{cq0}}{V_o} \cdot G_{pll} \\ 0 & \frac{v_{cd0}}{V_o} \cdot G_{pll} \end{bmatrix} \cdot \begin{bmatrix} \Delta v_{od} \\ \Delta v_{oq} \end{bmatrix} \quad (11)$$

where the steady-state values v_{cdq0} can be expressed as: $v_{cd0} = v_{od0} + R_f i_{cd0} - \omega L_f i_{cq0}$, and $v_{cq0} = v_{oq0} + R_f i_{cq0} + \omega L_f i_{cd0}$.

Moreover, the small-signal expression of the inner current control loop is provided by (12).

$$\begin{bmatrix} \Delta v_{cd}^* \\ \Delta v_{cq}^* \end{bmatrix} = \begin{bmatrix} G_{pi_l} & 0 \\ 0 & G_{pi_l} \end{bmatrix} \cdot \left(\begin{bmatrix} \Delta i_{cd}^* \\ \Delta i_{cq}^* \end{bmatrix} - \begin{bmatrix} \Delta i_{cd}^{ctrl} \\ \Delta i_{cq}^{ctrl} \end{bmatrix} \right) + \begin{bmatrix} 0 & -\omega L_f \\ \omega L_f & 0 \end{bmatrix} \cdot \begin{bmatrix} \Delta i_{cd}^{ctrl} \\ \Delta i_{cq}^{ctrl} \end{bmatrix} \quad (12)$$

where $G_{pi_l} = K_{p_id} + K_{i_id} / s = K_{p_iq} + K_{i_iq} / s$.

The small-signal expression of the outer power and AC voltage magnitude control loops is given by (13).

$$\begin{bmatrix} \Delta i_{cd}^* \\ \Delta i_{cq}^* \end{bmatrix} = \begin{bmatrix} -G_{pi_Vdc} & 0 \\ 0 & -G_{pi_Vo} \end{bmatrix} \cdot \left(\begin{bmatrix} \Delta(V_{dc}^2)^* \\ \Delta V_o^* \end{bmatrix} - \begin{bmatrix} \Delta(V_{dc}^2) \\ \Delta V_{oLPF} \end{bmatrix} \right) \quad (13)$$

where $G_{pi_Vdc} = K_{p_Vdc} + K_{i_Vdc} / s$ and $G_{pi_Vo} = K_{p_V} + K_{i_V} / s$.

Besides, the small-signal expression of the dc voltage dynamic on the dc-link capacitor can be derived as:

$$\Delta(V_{dc}^2) = \frac{(\Delta P_{in} - \Delta P_{out})}{sC_{dc} / 2} = G_{cdc} \cdot (\Delta P_{in} - \Delta P_{out}) \quad (14)$$

Moreover, the small-signal linearized expressions of the active power and the AC voltage amplitude feedbacks are shown as (15) and (16) respectively.

$$\begin{bmatrix} \Delta P_{out}^{ctrl} \\ 0 \end{bmatrix} = \begin{bmatrix} 3/2 \cdot i_{cd0} & 3/2 \cdot i_{cq0} \\ 0 & 0 \end{bmatrix} \cdot \begin{bmatrix} \Delta v_{od}^{ctrl} \\ \Delta v_{oq}^{ctrl} \end{bmatrix} + \begin{bmatrix} 3/2 \cdot V_o & 0 \\ 0 & 0 \end{bmatrix} \cdot \begin{bmatrix} \Delta i_{cd}^{ctrl} \\ \Delta i_{cq}^{ctrl} \end{bmatrix} \quad (15)$$

$$\begin{bmatrix} 0 \\ \Delta V_o^{ctrl} \end{bmatrix} = \begin{bmatrix} 0 & 0 \\ 1 & 0 \end{bmatrix} \cdot \begin{bmatrix} \Delta v_{od}^{ctrl} \\ \Delta v_{oq}^{ctrl} \end{bmatrix} \quad (16)$$

Furthermore, the small-signal expression of the first-order low-pass filter (LPF) is shown as (17).

$$G_{LPF} = \frac{\omega_{LPF}}{s + \omega_{LPF}} \quad (17)$$

where ω_{LPF} is the cut-off angular frequency of the LPF.

Overall, the 2×2 matrixes in (1), (2), (3), (9), (10), (11), (12), (13), (15) and (16) can be represented by \mathbf{B}_{lg} , \mathbf{B}_{cf} , \mathbf{B}_{lf} , \mathbf{B}_{pll-Vo} , \mathbf{B}_{pll-Ic} , \mathbf{B}_{pll-Vc} , \mathbf{B}_{pi-I} , \mathbf{B}_{decpl} , \mathbf{B}_{pi-Vv} , \mathbf{B}_i , \mathbf{B}_v and \mathbf{B}_{v1} respectively. Thus, the small-signal control structure of the dc voltage control scheme in Fig. 2 is shown in Fig. 4.

Similarly, for the power control scheme, the small-signal expression of the outer power and AC voltage magnitude control loops is given by (18).

$$\begin{bmatrix} \Delta i_{cd}^* \\ \Delta i_{cq}^* \end{bmatrix} = \begin{bmatrix} G_{pi_P} & 0 \\ 0 & -G_{pi_Vo} \end{bmatrix} \cdot \left(\begin{bmatrix} \Delta P^* \\ \Delta V_o^* \end{bmatrix} - \begin{bmatrix} \Delta P_{LPF} \\ \Delta V_{oLPF} \end{bmatrix} \right) \quad (18)$$

where $G_{pi_P} = K_{p_P} + K_{i_P} / s$.

The 2×2 matrix in (18) can be represented by \mathbf{B}_{pi-Pv} . Thus, the small-signal control structure of the power control scheme in Fig. 2 is shown in Fig. 5.

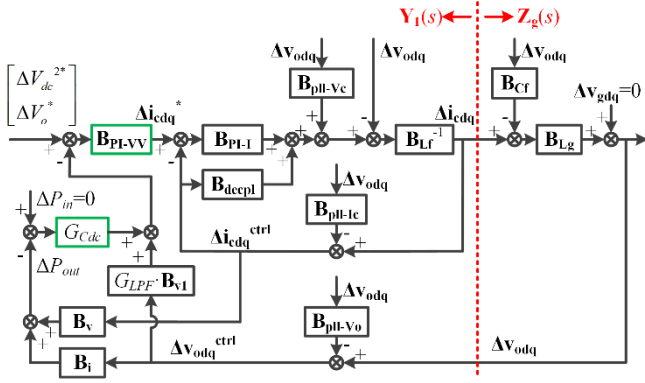


Fig. 4. Small-signal control structure of dc voltage control scheme.

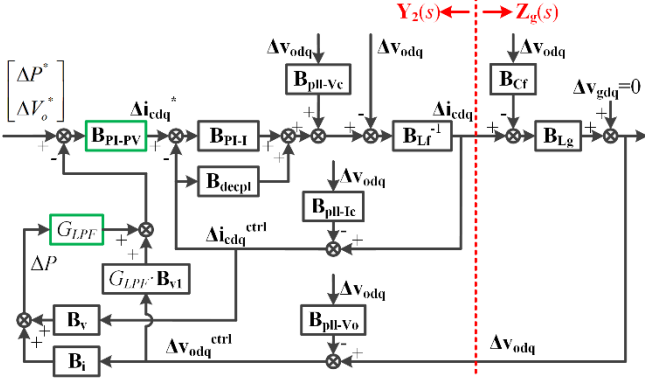


Fig. 5. Small-signal control structure of power control scheme.

It is known that the small-signal control structure can be represented by a Norton-Thevenin equivalent circuit. Thus, the equivalent admittance $\mathbf{Y}(s)$ and impedance $\mathbf{Z}_g(s)$ can be calculated respectively. And the matrix $\mathbf{Y}(s) \cdot \mathbf{Z}_g(s)$ can be used for the generalized Nyquist criterion (GNC) to analyze the stability of the system [13].

As shown in Fig. 4 and Fig. 5, the small-signal control structure can be divided into two parts. Considering Δv_{odq} as input and $-\Delta i_{cdq}$ as output for the converter-side subsystem, the equivalent admittance $\mathbf{Y}_1(s)$ and $\mathbf{Y}_2(s)$ can be derived as:

$$\mathbf{Y}_1(s) = (\mathbf{B}_{Lf} + \mathbf{B}_{PI-I} - \mathbf{B}_{decpI} - \mathbf{B}_{PI-I} \mathbf{B}_{PI-VV} G_{Cdc} \mathbf{B}_v)^{-1} \cdot [\mathbf{I} - (\mathbf{B}_{PI-I} - \mathbf{B}_{decpI} - \mathbf{B}_{PI-I} \mathbf{B}_{PI-VV} G_{Cdc} \mathbf{B}_v) \cdot \mathbf{B}_{pll-ic} - \mathbf{B}_{pll-vc} + \mathbf{B}_{PI-I} \mathbf{B}_{PI-VV} (G_{LPF} \mathbf{B}_{v1} - G_{Cdc} \mathbf{B}_i) (\mathbf{I} - \mathbf{B}_{pll-v0})] \quad (19)$$

$$\mathbf{Y}_2(s) = (\mathbf{B}_{Lf} + \mathbf{B}_{PI-I} - \mathbf{B}_{decpI} + \mathbf{B}_{PI-I} \mathbf{B}_{PI-PV} G_{LPF} \mathbf{B}_v)^{-1} \cdot [\mathbf{I} - (\mathbf{B}_{PI-I} - \mathbf{B}_{decpI} + \mathbf{B}_{PI-I} \mathbf{B}_{PI-PV} G_{LPF} \mathbf{B}_v) \cdot \mathbf{B}_{pll-ic} - \mathbf{B}_{pll-vc} + \mathbf{B}_{PI-I} \mathbf{B}_{PI-PV} (G_{LPF} \mathbf{B}_{v1} + G_{LPF} \mathbf{B}_i) (\mathbf{I} - \mathbf{B}_{pll-v0})] \quad (20)$$

Similarly, considering Δi_{cdq} as input and Δv_{odq} as output for the grid-side subsystem, the equivalent impedance $\mathbf{Z}_g(s)$ can be derived as:

$$\mathbf{Z}_g(s) = (\mathbf{B}_{Lg}^{-1} + \mathbf{B}_{Cr})^{-1} \approx \mathbf{B}_{Lg} \quad (21)$$

The control parameters can be designed as follows. Take $G_{pi-I} = \omega_i L_f + \omega_i R_f / s$, $G_{pi-Vdc} = C_{dc} / (3V_o) \cdot (0.8\omega_{dc} + 0.16\omega_{dc}^2 / s)$ and $G_{pi-Vo} = \omega_v I_{max} / V_o \cdot (1/\omega_{LPF} + 1/s)$, and $G_{pi-P} = \omega_p (1.5V_o) \cdot (1/\omega_{LPF} + 1/s)$, where ω_i and ω_v are the expected bandwidths of the current loop and AC voltage magnitude loop. ω_{dc} and ω_p are the expected bandwidths of the dc voltage loop and power loop for the two control schemes. Then, the equivalent admittance $\mathbf{Y}_1(s)$ and $\mathbf{Y}_2(s)$ can be derived as:

$$\mathbf{Y}_1(s) = \begin{bmatrix} Y_{1dd}(s) & Y_{1dq}(s) \\ Y_{1qd}(s) & Y_{1qq}(s) \end{bmatrix} \quad (22)$$

$$\mathbf{Y}_2(s) = \begin{bmatrix} Y_{2dd}(s) & Y_{2dq}(s) \\ Y_{2qd}(s) & Y_{2qq}(s) \end{bmatrix} \quad (23)$$

$$\left\{ \begin{aligned} Y_{1dd}(s) &= \frac{1}{sL_f + R_f} \frac{s}{s + \omega_i} + \frac{i_{cd0}}{V_o} \frac{G_{odc}}{s} \frac{\omega_i}{s + \omega_i} \\ &= \frac{1}{1 + \frac{G_{odc}}{s} \frac{\omega_i}{s + \omega_i}} \\ Y_{2dd}(s) &= \frac{1}{sL_f + R_f} \frac{s}{s + \omega_i} + \frac{i_{cd0}}{V_o} \frac{\omega_p}{s} \frac{\omega_i}{s + \omega_i} \\ &= \frac{1}{1 + \frac{\omega_p}{s} \frac{\omega_i}{s + \omega_i}} \end{aligned} \right. \quad (24)$$

where $G_{odc} = 2 \times 1 \times (\omega_{dc} / 2.5) + (\omega_{dc} / 2.5)^2 / s$.

$$\left\{ \begin{aligned} Y_{1dq}(s) &= \frac{i_{cq0}}{V_o} \frac{\frac{\omega_p}{s} \frac{\omega_i}{s + \omega_i} + \frac{(sL_f + R_f)\omega_i + sR_f}{(sL_f + R_f)(s + \omega_i)} G_{pll}}{1 + \frac{G_{odc}}{s} \frac{\omega_i}{s + \omega_i}} \\ Y_{2dq}(s) &= \frac{i_{cq0}}{V_o} \frac{\frac{\omega_p}{s} \frac{\omega_i}{s + \omega_i} + \frac{(sL_f + R_f)\omega_i + sR_f}{(sL_f + R_f)(s + \omega_i)} G_{pll}}{1 + \frac{\omega_p}{s} \frac{\omega_i}{s + \omega_i}} \end{aligned} \right. \quad (25)$$

$$Y_{1qd}(s) = Y_{2qd}(s) = \frac{-I_{max}}{V_o} \frac{\omega_v}{s} \frac{\omega_i}{s + \omega_i} \quad (26)$$

$$Y_{1qq}(s) = Y_{2qq}(s) = \frac{1 - G_{pll}}{sL_f + R_f} \frac{s}{s + \omega_i} - \frac{i_{cd0}}{V_o} \frac{(sL_f + R_f)\omega_i + sR_f}{(sL_f + R_f)(s + \omega_i)} G_{pll} \quad (27)$$

III. STABILITY ANALYSIS AND COMPARISON

Based on the parameters of a 30 kW grid-following inverter simulation platform (the parameters are listed in Table I), the stability of the two control schemes can be compared according to the GNC. For example, given two different steady-state operating points, stability analysis results of two control schemes are shown in Fig. 6 and Fig. 7 respectively. Fig. 6 shows the generalized Nyquist diagram of the matrix $\mathbf{Y}_1(s) \cdot \mathbf{Z}_g(s)$ based on (21) and (22). Fig. 7 shows the generalized Nyquist diagram of the matrix $\mathbf{Y}_2(s) \cdot \mathbf{Z}_g(s)$ based on (21) and (23).

It can be seen from Fig. 6 and Fig. 7 that the system is stable at 0.8 pu steady-state power by using both control schemes. However, it is unstable at 0.85 pu steady-state power. Thus, the stability boundary should be between 0.8 pu and 0.85 pu. Further, given different steady-state operating points, the stability boundary can be found. Stability boundaries of the dc voltage control scheme and the power control scheme are 0.81 pu and 0.82 pu when the SCR is 1.

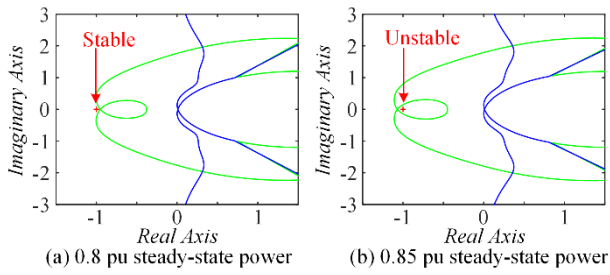


Fig. 6. Generalized Nyquist diagrams by using the small-signal impedance model of dc voltage control scheme with SCR = 1 and $\omega_{dc} = 100$ rad/s.

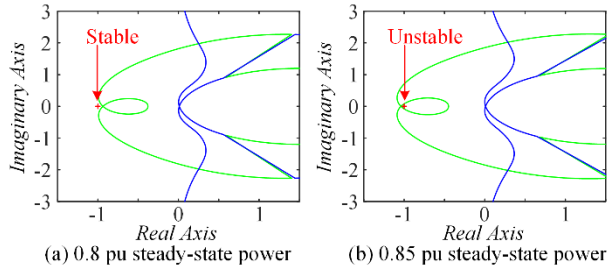


Fig. 7. Generalized Nyquist diagrams by using the small-signal impedance model of power control scheme with SCR = 1 and $\omega_p = 100$ rad/s.

TABLE I. PARAMETERS OF GRID-SIDE CONVERTER AND WEAK GRID

Parameters	Values
Grid phase voltage (peak value), V_g	311 V
Grid frequency, f_g	50 Hz
Rated power of inverter, S_N	30 kVA
Maximum current of inverter (peak value), I_{max}	64.3 A
DC-link voltage, V_{dc}	700 V
DC-link capacitor, C_{dc}	1 mF
Output filter inductor, L_f	5 mH
Output filter capacitor, C_f	5 μ F
R/X ratio of grid impedance, R_g/X_g	0.01
Short circuit ratio, SCR	1
Grid inductor, L_g	15.3 mH
Grid resistor, R_g	0.048 Ω
Switching/sampling frequency, f_s	10 kHz
Designed current-loop bandwidth, ω_i	1000 rad/s
Designed ac voltage-loop bandwidth, ω_v	50 rad/s
Designed dc voltage-loop bandwidth, ω_{dc}	10~100 rad/s
Designed power-loop bandwidth, ω_p	10~100 rad/s
Cut-off angular frequency of LPF, ω_{LPF}	200 rad/s
Damping ratio of PLL, ζ	1
Natural angular frequency of PLL, ω_n	20 rad/s

Similarly, when SCR is 2 and 3, stability boundaries can also be found. Thus, the stability boundaries of the two control schemes are shown in Fig. 8. It can be seen that the stability boundaries of the two control schemes are very close under different grid strengths when the power control loop and the dc voltage control loop bandwidths are the same.

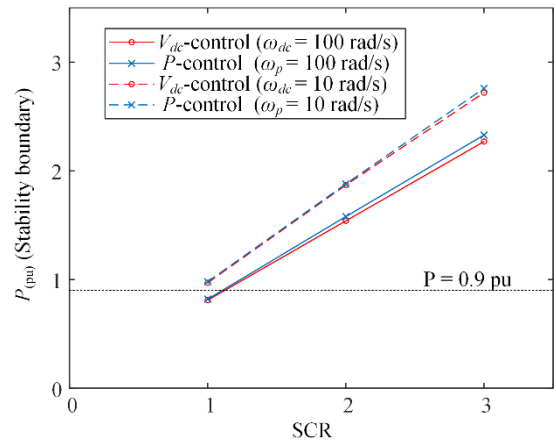


Fig. 8. Comparison of small-signal stability boundaries of dc voltage control scheme and power control scheme.

Moreover, it can be seen from Fig. 8 that the stability of both two control schemes can be enhanced by reducing the power loop or dc voltage loop bandwidth. For example, in the case of SCR = 1, when the bandwidths are reduced from 100 rad/s to 10 rad/s, the stability boundaries of the two control schemes can be improved from lower than 0.9 pu to higher than 0.9. Thus, a lower power loop or dc voltage loop bandwidth is beneficial to enhance the small-signal stability under weak grid conditions.

IV. SIMULATION VERIFICATION

In order to verify the correctness of the analyses above, the time-domain simulation model of a 30 kW grid-connected inverter is built in Matlab/Simulink. The system and control parameters are shown in Table I, which are the same as the parameters used for stability analyses. To avoid the influence of high-frequency harmonics, the average model of the inverter is used. Two bandwidths 100 rad/s and 10 rad/s for the dc voltage control and power control are used as examples for analysis. The simulation results of two control schemes with a higher power loop or dc voltage loop bandwidth (i.e. 100 rad/s) are shown in Fig. 9. Besides, the simulation results of two control schemes with a lower power loop or dc voltage loop bandwidth (i.e. 10 rad/s) are shown in Fig. 10.

It can be seen from Fig. 9 that both two control schemes are unstable when the active power is 0.9 pu under the condition of SCR = 1 and $\omega_p = \omega_{dc} = 100$ rad/s. On the contrary, as shown in Fig. 10, both two control schemes are stable when the active power is 0.9 pu in the case of SCR = 1 and $\omega_p = \omega_{dc} = 10$ rad/s. These simulation results agree well with the stability analysis results presented in Fig. 8.

Moreover, the overvoltage problem on the dc-link capacitor can be observed in Fig. 10(a). Because a lower dc voltage loop bandwidth is used, the output power changes more slowly than the input power. Thus, the short-term energy on the dc-link capacitor makes the dc voltage increase, which may cause the overvoltage problem. This is risky to damage the dc-link capacitor. Therefore, a higher dc voltage loop bandwidth is beneficial to avoid the overvoltage problem. Thus, for the dc voltage control scheme, the dc voltage loop bandwidth cannot be designed too low and it needs a trade-off between the stability and the overvoltage problem. Differently, as shown in Fig. 10(b), there is no such a problem to limit the power loop bandwidth of the power control scheme. Therefore, a lower power loop bandwidth can be used for the power control scheme to enhance stability.

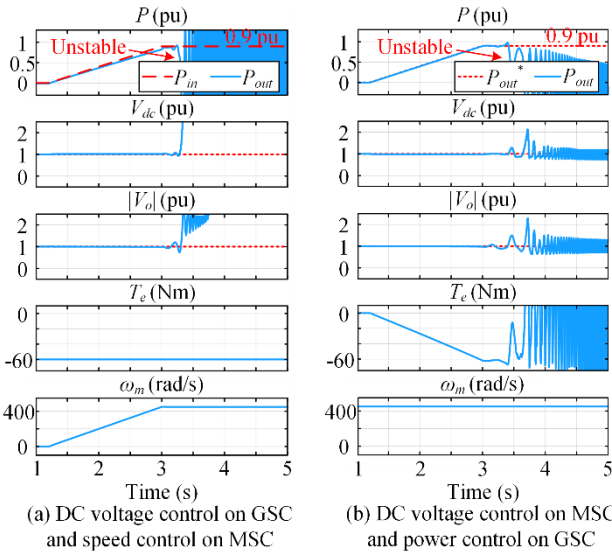


Fig. 9. Simulation results of dc voltage control scheme and power control scheme on GSC with $\omega_p = \omega_{dc} = 100$ rad/s and SCR = 1.

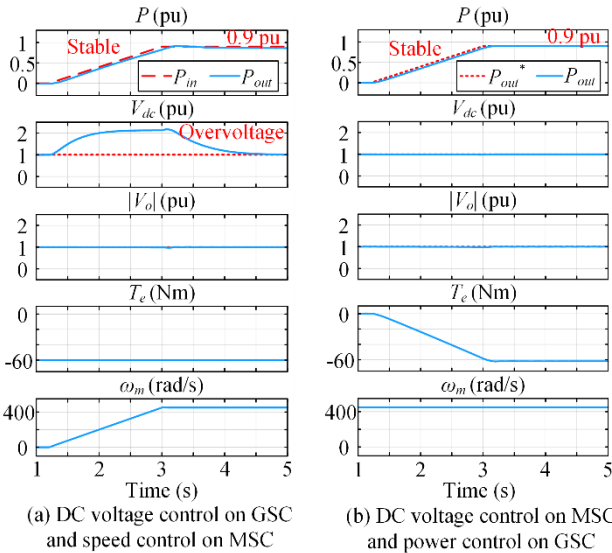


Fig. 10. Simulation results of dc voltage control scheme and power control scheme on GSC with $\omega_p = \omega_{dc} = 10$ rad/s and SCR = 1.

Furthermore, it is worth mentioning that this paper mainly discusses voltage stability. However, frequency stability is also important for the power grid. The grid-forming control scheme on the GSC is an effective solution to support the grid frequency [16]. Thus, the machine-side dc voltage control is necessary to realize the grid-forming control on the GSC [17]. In this case, the MPPT control may be discarded. Overall, the authors believe that the machine-side dc voltage control scheme on type-4 wind generation systems will be more popular in future power grids with high percentages of renewable energy sources.

V. CONCLUSION

The comparison of the machine-side dc voltage control and the grid-side dc voltage control of type-4 wind generation systems are the main focus of this paper. By comparing the typical dc voltage control and the power control schemes on the GSC, it is revealed that the small-signal stability of the two control schemes is basically the same when using the same control loop bandwidths. Even so, the power control scheme

on the GSC (dc voltage is controlled by MSC) is preferable to be used in weak grids, because a lower power loop bandwidth of the power control scheme can be designed to improve the small-signal stability. However, for the dc voltage control scheme on the GSC, the dc voltage loop bandwidth cannot be designed too low due to the overvoltage problem on the dc-link capacitor. Therefore, from the small-signal stability perspective, the dc voltage control on the MSC is better than the GSC under weak grid conditions.

REFERENCES

- [1] F. Blaabjerg, Y. Yang, D. Yang and X. Wang, "Distributed power-generation systems and protection," *Proc. IEEE*, vol. 105, no. 7, pp. 1311-1331, Jul. 2017.
- [2] X. Wang and F. Blaabjerg, "Harmonic stability in power electronic-based power systems: concept, modeling, and analysis," *IEEE Trans. Smart Grid*, vol. 10, no. 3, pp. 2858-2870, May 2019.
- [3] J. A. Suul, S. D'Arco, P. Rodriguez, and M. Molinas, "Impedance-compensated grid synchronization for extending the stability range of weak grids with voltage source converters," *IET Gen., Trans. Distr.*, vol. 10, no. 6, pp. 1315-1326, Apr. 2016.
- [4] B. Wen, D. Boroyevich, R. Burgos, P. Mattavelli and Z. Shen, "Analysis of D-Q small-signal impedance of grid-tied inverters," *IEEE Trans. Power Electron.*, vol. 31, no. 1, pp. 675-687, Jan. 2016.
- [5] J. F. Morris, K. H. Ahmed and A. Egea-Alvarez, "Analysis of controller bandwidth interactions for vector-controlled VSC connected to very weak AC grids," *IEEE J. Emerg. Sel. Top. Power Electron. (Early Access)*, Oct. 2020.
- [6] J. Xi, H. Geng, G. Yang and S. Ma, "Inertial response analysis of PMSG-based WECS with VSG control," *J. Eng.*, vol. 2017, no. 13, pp. 897-901, Dec. 2017.
- [7] Y. Xu, M. Zhang, L. Fan and Z. Miao, "Small-signal stability analysis of type-4 wind in series-compensated networks," *IEEE Trans. Energy Conv.*, vol. 35, no. 1, pp. 529-538, March 2020.
- [8] H. Yuan, X. Yuan and J. Hu, "Modeling of grid-connected VSCs for power system small-signal stability analysis in DC-Link voltage control timescale," *IEEE Trans. Power Syst.*, vol. 32, no. 5, pp. 3981-3991, Sep. 2017.
- [9] S. Rezaee, A. Radwan, M. Moallem and J. Wang, "Voltage source converters connected to very weak grids: accurate dynamic modeling, small-signal analysis, and stability improvement," *IEEE Access*, vol. 8, pp. 201120-201133, Nov. 2020.
- [10] D. Lu, X. Wang and F. Blaabjerg, "Impedance-based analysis of DC-link voltage dynamics in voltage-source converters," *IEEE Trans. Power Electron.*, vol. 34, no. 4, pp. 3973-3985, Apr. 2019.
- [11] L. Fan and Z. Miao, "Wind in weak grids: 4 Hz or 30 Hz oscillations?," *IEEE Trans. Power Syst.*, vol. 33, no. 5, pp. 5803-5804, Sep. 2018.
- [12] Y. Xu, H. Nian and L. Chen, "Small-signal modeling and analysis of DC-link dynamics in type-IV wind turbine system," *IEEE Trans. Ind. Electron.*, vol. 68, no. 2, pp. 1423-1433, Feb. 2021.
- [13] L. Huang, C. Wu, D. Zhou, and F. Blaabjerg, "Comparison of three small-signal stability analysis methods for grid-following inverter," *Int. Conf. Opt. Electr. Electron. Equip. (OPTIM)*, 2021, in press.
- [14] L. Huang, C. Wu, D. Zhou, and F. Blaabjerg, "A simple impedance reshaping method for stability enhancement of grid-following inverter under weak grid," *IEEE 12th Int. Symp. Power Electron. Distr. Gen. (PEDG)*, pp. 1-6, 2021.
- [15] L. Huang, C. Wu, D. Zhou, and F. Blaabjerg, "Impact of grid strength and impedance characteristics on the maximum power transfer capability of grid-connected inverters," *Appl. Sci.*, vol. 11, no. 9, p. 4288, May 2021.
- [16] T. Lund, B. Yin, G. K. Andersen, M. Gupta, "Challenges and solutions for integration of wind power in weak grid areas with high inverter penetration," *19th Wind Integ. Workshop*, pp. 1-8, Nov. 2020.
- [17] J. Kim, S. H. Lee and J. Park, "Inertia-free stand-alone microgrid - part II: inertia control for stabilizing DC-link capacitor voltage of PMSG wind turbine system," *IEEE Trans. Ind. Appl.*, vol. 54, no. 5, pp. 4060-4068, Sep.-Oct. 2018.